PASJ: Publ. Astron. Soc. Japan , 1–**??**,
© 2009. Astronomical Society of Japan.

arXiv:0906.0227v1 [astro-ph.GA] 1 Jun 2009

NH_3 in the Galactic Center is formed in Cool Conditions

Takumi Nagayama,[1,6] Toshihiro Omodaka,[2] Toshihiro Handa,[3]
Hideyuki Toujima,[1,6] Yoshiaki Sofue,[2] Tsuyoshi Sawada,[4]
Hideyuki Kobayashi,[5] and Yasuhiro Koyama[6]
[1] *Graduate School of Science and Engineering, Kagoshima University,*
1-21-35 Kôrimoto, Kagoshima 890-0065
[2] *Faculty of Science, Kagoshima University, 1-21-35 Kôrimoto, Kagoshima 890-0065*
[3] *Institute of Astronomy, University of Tokyo, 2-21-1 Osawa, Mitaka, Tokyo 181-0015*
[4] *ALMA Project Office, National Astronomical Observatory of Japan,*
2-21-1 Osawa, Mitaka, Tokyo 181-8588
[5] *Mizusawa VERA Observatory, National Astronomical Observatory of Japan,*
2-21-1 Osawa, Mitaka, Tokyo 181-8588
[6] *Kashima Space Research Center, National Institute of Information and Communications Technology,*
893-1 Hirai, Kashima, Ibaraki 314-8501
nagayama@astro.sci.kagoshima-u.ac.jp

(Received 2008 December 4; accepted)

Abstract

It is an open question why the temperature of molecular gas in the Galactic center region is higher than that of dust. To address this problem, we made simultaneous observations in the NH_3 $(J,K) = (1,1)$, (2,2), and (3,3) lines of the central molecular zone (CMZ) using the Kagoshima 6 m telescope. The ortho-to-para ratio of NH_3 molecules in the CMZ is 1.5–3.5 at most observed area. This ratio is higher than the statistical equilibrium value, and suggests that the formation temperature of NH_3 is 11–20 K. This temperature is similar to the dust temperature estimated from the submillimeter and infrared continuum. This result suggests that the NH_3 molecules in the CMZ were produced on dust grains with the currently observed temperature (11–20 K), and they were released into the gas phase by supernova shocks or collisions of dust particles. The discrepancy between warm molecular gas and cold dust can be explained by the transient heating of the interstellar media in the CMZ approximately 10^5 years ago when the NH_3 molecules were released from the dust.

Key words: Galaxy:center - Interstellar:molecules - Interstellar:ammonia

1. Introduction

It is one of the biggest questions why the temperature of molecular gas in the CMZ is much higher than that of dust. Many molecular line observations have revealed that the temperature of molecular gas is higher than that of dust in the Galactic center region (Nagayama et al. 2007, Paper I and references therein). It is inconsistent with the standard molecular gas heating model because there interstellar gas is mainly heated up by hot dust. Surveys in NH_3 $(J,K) = (1,1)$ and (2,2) lines have revealed that this inconsistency is not confined to small regions; in fact, it extends over the entire molecular cloud complex in the Galactic center, called the CMZ. This implies that a gas heating process over a hundred parsec scale differs from that in the galactic disk.

To address this problem, the abundance ratio of ortho-NH_3 to para-NH_3, ortho-to-para ratio, is a key. An NH_3 molecule has two different structures. One is called ortho-NH_3, and the other para-NH_3 which are different in relative orientation of the three hydrogen spins with respect to the nitrogen spin. Ortho-NH_3 emits $K = 3n$ $(n = 0,\ 1,\ 2,\ \cdots)$ lines while para-NH_3 emits $K \neq 3n$ $(n = 0,\ 1,\ 2,\ \cdots)$ lines. Ortho-NH_3 and para-NH_3 are kept for a long time ($\sim 10^6$ yr) because no collisional or fast radiative process can transform between these two configurations of NH_3. The ortho-to-para ratio is expected to be the statistical equilibrium value of 1.0 when NH_3 molecules are formed in the processes of gas phase reactions under high temperature. The ortho-to-para ratio is expected to be larger than unity when NH_3 molecules adsorbed on cold dust grain surfaces are released into the gas phase with excess desorption energy, which is comparable to the energy difference between the ortho and para states (Umemoto et al. 1999). Therefore, the ortho-to-para ratio indicates the physical conditions in which NH_3 molecules are formed. Moreover, NH_3 molecules formed on a dust grain surface colder than 100 K cannot be released to interstellar gas without the heating of dust (Sandford & Allamandola 1993). NH_3 molecules with a low formation temperature indicate that dust should be heated up by some process such as the passage of a shock wave (Umemoto et al. 1999).

In the CMZ, the (3,3) emission is stronger than the (1,1) and (2,2) emissions (Morris et al. 1983). This indicates that ortho-NH_3 is overabundant as compared to para-NH_3. However, the ortho-to-para ratio of NH_3 over the entire CMZ has not yet been obtained. We aim to clarify the formation mechanism of molecular gas in the CMZ by simultaneous observations in NH_3 (1,1), (2,2), and (3,3) lines and by estimating the ortho-to-para ratio.

We present large-scale maps of the CMZ in the NH_3 (1,1), (2,2), and (3,3) lines. In section 2, we describe our observations in detail. The observed data are presented in section 3. In section 4, we discuss the physical conditions of the CMZ through measurements of the rotational temperature and the ortho-to-para ratio in NH_3 lines. In this paper, we assume that the distance to the Galactic center is 8.5 kpc and we use the direction on the sky based on the galactic coordinates.

2. Observations

2.1. Data Obtained Using the Kagoshima 6 m Telescope

We conducted a large-scale survey using the Kagoshima 6 m telescope of the National Astronomical Observatory of Japan (NAOJ) from September 2005 to March 2007. We made simultaneous observations in the NH_3 $(J,K) =$ (1,1), (2,2), and (3,3) lines at rest frequencies of 23.694495, 23.722633, and 23.870129 GHz, respectively. At 23 GHz, the telescope beamwidth was $9\overset{\prime}{.}5$ and the main beam efficiency ($\eta_{\rm MB}$) was 0.54. We used a K-band HEMT amplifier whose system noise temperature was 200–300 K. All spectra were obtained using a 8192-channel FX-type software-based spectrometer developed by the Kagoshima University and the National institute of Information and Communications Technology (NiCT). The bandwidth and frequency resolution of the spectrometer are 256 MHz and 31.25 kHz, respectively. At the NH_3 frequencies, these correspond to a velocity coverage and velocity resolution of 3200 km s^{-1} and 0.39 km s^{-1}, respectively. We obtained 471 NH_3 (1,1), (2,2) and (3,3) spectra at $-1\overset{\circ}{.}000 \le l \le 2\overset{\circ}{.}000$ and $-0\overset{\circ}{.}375 \le b \le +0\overset{\circ}{.}375$ with a spacing of $0\overset{\circ}{.}125$. The surveyed area corresponds to 450×110 pc. The NH_3 (1,1) and (2,2) data presented in this paper were newly observed, although we have already observed them, as shown in Paper I. To obtain intensity ratios from (2,2) to (1,1) and (3,3) to (1,1) accurately, we simultaneously observed three lines. The data shown in Paper I are not included the analysis in this paper.

All data were obtained by position switching between the target positions and reference positions. The reference positions are at the Galactic latitude $b < -1^\circ$, where no NH_3 emission was detected. We integrated at least 30 min at each point. The relative pointing error was better than $1'$, which was verified by the observations of several H_2O (frequency; 22.235080 GHz) maser sources.

Data reduction was performed using the UltraSTAR package developed by the radio astronomy group at the University of Tokyo (Nakajima et al. 2007). To improve the signal-to-noise ratio, the obtained spectra are smoothed to a velocity resolution of 5 or 10 km s^{-1}. The rms noise level after smoothing to 5 km s^{-1} is typically 0.030 K in unit of the main beam brightness temperature defined by $T_{\rm MB} \equiv T_{\rm A}^*/\eta_{\rm MB}$, where $T_{\rm A}^*$ is the antenna temperature calibrated by the chopper wheel method (Kutner & Ulich 1981). This sensitivity is better than that in the data shown in Paper I by a factor of 2.7. In this paper, the intensities are presented in the main beam temperature.

2.2. Data Obtained Using the Kashima 34 m Telescope

In order to conduct an investigation of the "$0\overset{\circ}{.}9$ wing feature", which is a high-velocity wing at $l \sim 0\overset{\circ}{.}9$ at higher resolution (see section 4.5.5), we observed the area at $0\overset{\circ}{.}700 \le l \le 0\overset{\circ}{.}940$ and $-0\overset{\circ}{.}180 \le b \le +0\overset{\circ}{.}020$ with a spacing of $0\overset{\circ}{.}040$. This observation was made using the $1\overset{\prime}{.}6$ beam of the Kashima 34 m telescope of NiCT from May to November in 2007. The spectra in the NH_3 (1,1), (2,2), and (3,3) lines were obtained by the same method as that used in the Kagoshima 6 m telescope survey. We integrated at least 5 min at each point. The rms noise level after 5 km s^{-1} smoothing is typically 0.064 K in $T_{\rm MB}$.

3. Results

3.1. Profiles

Direct information about the observed lines can be seen in each line profile. Significant NH_3 (1,1), (2,2), and (3,3) emissions for which the signal-to-noise ratio exceeds 3 were detected for 101, 84, and 97 positions out of 157 observed positions, respectively. The observed profiles in the (1,1), (2,2), and (3,3) lines toward four prominent positions [Sgr C $(l,\ b) = (-0\overset{\circ}{.}500,\ -0\overset{\circ}{.}125)$, Sgr A $(0\overset{\circ}{.}125,\ -0\overset{\circ}{.}125)$, Sgr B $(0\overset{\circ}{.}750,\ -0\overset{\circ}{.}125)$, and $1\overset{\circ}{.}3$ region $(1\overset{\circ}{.}250,\ -0\overset{\circ}{.}125)$] are shown in Figure 1. The (2,2) line is the weakest, and the (3,3) line is the strongest at most positions, especially near the velocity of peak intensity.

The line shapes of the three transitions are similar. Although an NH_3 line profile has five quadruple hyperfine lines, we cannot separate these components due to the large internal motion of the gas in an observed beam. The line shapes reflect the violent motion of the gas .

3.2. Intensity Distributions over the Entire CMZ

To figure out the NH_3 gas distribution on the sky over the entire CMZ, the velocity integrated intensity distribution is useful for comparison with the maps observed in radio and infrared continuum emissions. Figure 2 shows the l-b maps of intensities, velocity-integrated in the range of $v_{\rm LSR} = -200$ to 200 km s^{-1}, covering the NH_3 emission.

The observed area is extended to $l > 1\overset{\circ}{.}6$ from the previous survey (Paper I) along the galactic plane. The distributions in the (1,1) and (2,2) lines are consistent with those shown in Paper I; in addition, fainter peaks and diffuse emission were detected because of the improved sensitivity. The total integrated intensities in the (1,1), (2,2), and (3,3) lines of the entire observed area are 1693, 1159, and 2120 K km s^{-1}, respectively.

The (3,3) line is emitted by the ortho-NH_3. The (1,1) and (2,2) lines are emitted by the para-NH_3. Ortho and para-NH_3 cannot be transformed by collisional or fast radiative process in the interstellar gas. This implies that the ortho- and para-NH_3 molecules can be dealt with as different molecular species. Therefore, the similarity of the intensity distribution in the (3,3) line with those in the (1,1) and (2,2) lines should contain some astrophysical information.

The *l*-*b* maps in the NH_3 lines appear similar to other molecular lines such as those of CO (Sawada et al. 2001) and CS (Tsuboi et al. 1999). This similarity is not only in the sky distribution but in the *l*-*v* domain. Figure 3 shows *l*-*v* diagrams of three transitions integrated over the observed latitudes and Figure 4 shows the *l*-*v* diagrams at a fixed latitude. Even for $v_{\rm LSR} = 0$ km s^{-1}, the NH_3 lines are not affected by foreground absorption; in contrast, the effect is significant in the CO line. Due to the difference of the critical densities, the CO line traces lower-density gas whereas the NH_3 line traces only higher-density gas, $n({\rm H_2}) \sim 10^4$ cm^{-3}. The NH_3 and CO lines trace the different density gas microscopically. Therefore, morphological similarity suggests that the flux ratio of core to envelope in an observed beam is almost uniform over the CMZ. Moreover, the fairly large optical depths in both lines ($\tau \lesssim 2$–4) may reduce the morphological difference, because both lines mainly trace the outer envelope of the cloud complex.

3.3. *Observational Properties of Individual Clouds*

To investigate the gas properties at various locations in the CMZ, we divide the intensity distribution into several small regions and define a *cloud* as a single peak in the *l*-*v* and *b*-*v* distributions, with the intensities stronger than the 3 σ level (> 0.1 K in $T_{\rm MB}$) in all three lines. Based on this definition, we identified 13 clouds. The total integrated intensity of these 13 clouds is 3447 K km s^{-1}, which corresponds to 69% of the integrated intensity of the entire observed area. Therefore, the majority of the NH_3 gas in the CMZ is traced by these clouds. The peak positions, apparent sizes, and line widths of these clouds are listed in Table 1. We defined their sizes and widths (Δl, Δb, and Δv) as apparent full widths at half-maximum (FWHM) of the main-beam temperature without beamsize deconvolution. The integrated intensities of the clouds are shown in Table 2.

Four major clouds of the CMZ are seen in the NH_3 maps (from west to east: the Sgr A 20 km s^{-1} cloud at $l \simeq -0.^\circ1$, the Sgr A 40 km s^{-1} cloud at $l \simeq 0.^\circ1$, the Sgr B cloud at $l \simeq 0.^\circ7$, and the $1.^\circ3$ region cloud at $l \simeq 1.^\circ3$). These clouds were also detected in the previous observation (Paper I), and their locations and extents are found to be the same with those of the previous ones. In our new map, we clearly detected the NH_3 clouds associated with the Sgr C H II region at $(l,\, b,\, v_{\rm LSR}) \simeq (-0.^\circ5,\ -0.^\circ1,\ -50$ km s$^{-1})$ and a part of the expanding molecular ring (EMR) at $(l,\, b,\, v_{\rm LSR}) \simeq (-0.^\circ9,\ -0.^\circ1,\ 140$ km s$^{-1})$. Both had been marginally detected in the previous observation.

3.4. *Intensity Ratios*

The intensity ratio of the (2,2) line to the (1,1) line, $R_{(2,2)/(1,1)}$, is determined by the optical depth, τ, and the kinetic temperature, $T_{\rm k}$, of the gas. With a given optical depth, the rotational temperature of the transition, $T_{\rm rot}$, can be derived from the $R_{(2,2)/(1,1)}$ and it gives the gas kinetic temperature. Therefore, the changing line ratios indicate the differences of the rotational temperature.

Figure 5(a) shows the histograms of ratio for the integrated intensity over the entire observed area with 3 σ detection in both the (1,1) and (2,2) lines after smoothing to 10 km s^{-1}. The value of $R_{(2,2)/(1,1)}$ ranges between 0.4 and 1.5. The mean value and standard deviation of $R_{(2,2)/(1,1)}$ are derived to be 0.70 and 0.15, respectively. The NH_3 integrated intensity with $R_{(2,2)/(1,1)} = 0.4$–0.8 and $R_{(2,2)/(1,1)} > 0.8$ are 82% and 18% of the total NH_3 integrated intensity, respectively. These values are consistent with the results described in Paper I.

The intensity ratio of the (3,3) line to the (1,1) line, $R_{(3,3)/(1,1)}$, is determined by the relative abundance of the ortho-to-para NH_3, $R_{\rm o/p}$, and the kinetic temperature. In the case that ortho-NH_3 and para-NH_3 have the same kinetic temperature, $R_{(3,3)/(1,1)}$ increases with $R_{\rm o/p}$. In the case that the ortho-to-para ratio is uniform, $R_{(3,3)/(1,1)}$ increases with the kinetic temperature. We can estimate the ortho-to-para ratio using the kinetic temperature obtained by the $R_{(2,2)/(1,1)}$. The ortho-to-para ratio depends on the temperature when NH_3 molecules are formed. The ortho-to-para ratio increases in the case that NH_3 molecules are produced in low temperature conditions (e.g., more than 10 at 5 K) (Takano et al. 2002). $R_{(3,3)/(1,1)}$ is the direct observed value that is related to the ortho-to-para ratio, and therefore, it should be studied in detail.

The (3,3) emission is stronger than the (1,1) emission at most observed positions. The NH_3 integrated intensity for $R_{(3,3)/(1,1)} > 1$ is 90% of the total NH_3 intensity. The histogram of $R_{(3,3)/(1,1)}$ is shown in Figure 5(b). The mean value and standard deviation of $R_{(3,3)/(1,1)}$ are derived to be 1.28 and 0.29, respectively. $R_{(3,3)/(1,1)}$ of the CMZ is higher than that of typical molecular clouds in the galactic disk. In galactic disk clouds, $R_{(3,3)/(1,1)}$ as high as that observed in the CMZ is found only in active and massive star-forming regions (see section 4.2).

To investigate the spatial distributions of $R_{(2,2)/(1,1)}$ and $R_{(3,3)/(1,1)}$, we show the *l*-*v* diagrams of $R_{(2,2)/(1,1)}$ and $R_{(3,3)/(1,1)}$ superimposed on the (1,1) emission integrated over the entire observed latitude in Figure 6. The values of $R_{(2,2)/(1,1)}$ and $R_{(3,3)/(1,1)}$ vary with the location. The high-ratio region is common in both the ratios. Although the kinematical timescale significantly depends on the galactocentric distance, neither ratio exhibits any systematic structure dependent on the distance from the Galactic center. Overall, the distributions of $R_{(2,2)/(1,1)}$ and $R_{(3,3)/(1,1)}$ are similar. However, some regions such as the Sgr C cloud near $l \simeq -0.^\circ5$ exhibit a much lower $R_{(3,3)/(1,1)}$.

4. Discussion

4.1. *Physical Properties of Molecular Gas in CMZ*

$T_{\rm k}$ derived from the $R_{(2,2)/(1,1)}$ is thought to be the current temperature of the gas. The temperature derived from the ortho-to-para ratio corresponds to the temperature when the NH_3 molecules were formed (Umemoto et al. 1999). These two temperatures can be obtained from the NH_3 observations. In the case that the entire interstellar matter is under thermal equilibrium and in a steady state, the two temperatures are the same.

We derived the $T_{\rm k}$ of the gas under the cases of optically thin ($\tau \ll 1$) and thick ($\tau \sim 3$) using the same method as that described in Paper I. The gas is warmer than the dust ($T_{\rm dust} = 15$–22 K; Lis et al. 2001) at most observed positions, which is consistent with the conclusion shown in Paper I. The $R_{(2,2)/(1,1)} = 0.4$–0.8 and $R_{(2,2)/(1,1)} > 0.8$ correspond to $T_{\rm k} \simeq 20$–80 K and $T_{\rm k} > 80$ K, respectively. The gases corresponding to $T_{\rm k}$ values of 20–80 K and > 80 K contain 82% and 18% of the total NH_3 integrated intensity in the entire observed area, respectively. The higher ratio ($R_{(2,2)/(1,1)} \geq 0.7$) components are located at $l \simeq -0.^\circ5$, $0.^\circ0$, $0.^\circ9$, and $1.^\circ3$ (Figure 6(a)). These locations coincide with those of high CO $J = 3$–$2/J = 1$–0 ratios ($R_{\rm CO3-2/1-0} \geq 1.5$; Oka et al. 2007). This supports the notion that the components with higher $R_{(2,2)/(1,1)}$ values trace the high-temperature gas. $R_{(2,2)/(1,1)} \geq 0.7$ corresponds to $T_{\rm k} \geq 60$ K in the optically thin case and ≥ 40 K in the optically thick case ($\tau \sim 3$). This is consistent with $R_{\rm CO3-2/1-0} \geq 1.5$ corresponding to $T_{\rm k} \geq 48$ K, which is derived from a large velocity gradient (LVG) calculation (Oka et al. 2007).

The high $R_{(3,3)/(1,1)}$ value in the CMZ indicates that the ortho-NH_3 is overabundant as compared to para-NH_3. To obtain the ortho-to-para ratio, we estimated the column densities using the rotation diagram method under the optically thin assumption. We derived the column densities of each level from the integrated intensities. The procedure is based on Takano et al. (2002). Although the optical depth of the NH_3 lines in the CMZ is moderate ($\tau \leq 2$–4; Hüttemeister et al. 1993; Paper I). and the ortho-to-para ratio changes with the optical depth, the value obtained under the optically thin assumption can provide the lower limit of the ortho-to-para ratio ($R_{\rm o/p} = 2$ at $\tau \ll 1$ corresponds to $R_{\rm o/p} = 6$ at $\tau = 3$).

Because of the absence of emission lines from molecules at the (0,0) level, we cannot obtain the column density of the (0,0) level directly. However, we can derive the column density of the NH_3 at the (0,0) level under the assumption that the ortho- and para-NH_3 molecules are thermalized at the same rotational temperature derived from the $R_{(2,2)/(1,1)}$. This assumption is a better approximation than using the rotational temperature between (3,3) and (6,6), because the (1,1) and (2,2) levels are between the (0,0) and (3,3) levels. The energies of the (3,3) and (6,6) levels are 124.5 K and 412.4 K above the ground state, respectively. The large energy difference between the (3,3) and (6,6) levels suggests that the (3,3) and (6,6) emissions originate from different components.

We calculated the column densities of ortho-NH_3 and para-NH_3 by the formulas $N(\text{ortho}) = N(0,0) + N(3,3)$ and $N(\text{para}) = N(1,1) + N(2,2)$, respectively. The column densities of the levels higher than (4,4) are less than 2% of those of the (0,0) and (1,1) levels when the rotational temperature is 36 K, which is estimated from the mean $R_{(2,2)/(1,1)} = 0.70$. We considered only the metastable states ($J = K$), because transitions from non-metastable states ($J \neq K$) to metasable states are generally quite rapid.

Figure 7 shows histograms of the ortho-to-para ratio for the integrated intensity over the entire observed area with 10 σ detection in the (1,1), (2,2), and (3,3) lines after smoothing to 10 km $\rm s^{-1}$. The mean value and the standard deviation of $R_{\rm o/p}$ are derived to be 2.0 and 0.6, respectively. To investigate the spatial distributions of the ortho-to-para ratio, we have plotted the ortho-to-para ratio on the l-v plane, as shown in Figure 8. We found that the ortho-to-para ratio varies with the location, and it does not exhibit systematic structures dependent on the distance from the Galactic center nor the core/envelope of clouds.

The distributions of $R_{(2,2)/(1,1)}$ and $R_{(3,3)/(1,1)}$ appear similar on the l-v plane (Figure 6). To see this correlation quantitatively, we made a correlation plot of $R_{(2,2)/(1,1)}$ and $R_{(3,3)/(1,1)}$, as shown in Figure 9. $R_{(3,3)/(1,1)}$ depends on both $R_{\rm o/p}$ and $T_{\rm rot}$, although $R_{(2,2)/(1,1)}$ depends on only $T_{\rm rot}$. Therefore, we can draw curves of constant $R_{\rm o/p}$ values on the $R_{(2,2)/(1,1)}$-$R_{(3,3)/(1,1)}$ domain (Figure 9). Figure 9 shows the curves with $R_{\rm o/p} = 1$, 2, 4, and 6. Figure 9 shows also a plot of the observed ratios of the clouds in the galactic disk obtained from other observations. Most galactic disk clouds such as M17, Cep A, and NGC 7538, show $R_{\rm o/p} \simeq 1$, although intense and massive starforming cores such as W49 and W51 are located along the curve with $R_{\rm o/p} \simeq 4$. The CMZ is close to the latter and is different from the former. This suggests that the entire CMZ should be under physical conditions as similar to an intense starforming core.

It has been reported that the ortho-to-para ratios of nearby external galaxies are as high as that of the CMZ. The ortho-to-para ratios of Maffei 2, Arp 220, and NGC 253 are 2.6, 1.7, and 6.2, respectively (Takano et al. 2000; 2002; 2005). We calculated the orhto-to-para ratios of IC 342 and M 82 using the data of Mauersberger et al. (2003) and Weiß et al. (2001), respectively. These have been plotted in Figure 9. From these data, IC 342 exhibits lower $R_{\rm o/p}$ as compared to that of other galaxies. However, $R_{\rm o/p}$ of IC 342 is calculated to be 1.8 ± 0.5 from the data obtained using the NRO 45 m telescope (S. Takano, 2008 private communication). Therefore, IC 342 may actually have a high $R_{\rm o/p}$ value.

M82 also shows low $R_{\rm o/p}$. Usero et al. (2007) suggests that the evolutionary stage of the starburst in M 82 is different from those of NGC 253 and IC 342. This difference may relate to the low ortho-to-para ratio in M 82.

The ortho-to-para ratio is $\gtrsim 2$ for the CMZ and most of external galaxies. We conclude that the ortho-to-para ratio of the CMZ and the central region of the galaxies is higher than that of galactic disk.

4.2. *Origin of NH_3*

The ortho-to-para ratio is related to the temperature when NH_3 molecules are formed. The ortho-to-para ratio approaches unity when NH_3 molecules are produced under high temperature (≥ 40 K) conditions. This ratio increases when NH_3 molecules are produced and equilibrated at low temperature (e.g., more than 10 at 5 K). This is because most of molecules then reside in the lowest state, or the (0,0) ortho level. The relationship between the ortho-to-para ratio and the formation temperature is shown in Figure 3 of Takano et al. (2002). Our observation shows the ortho-to-para ratio is 1.5–3.5 for 95% of the total integrated intensity of the entire CMZ (Figure 7). This ratio corresponds to a formation temperature of 11–20 K. This is much lower than the gas kinetic temperature derived from $R_{(2,2)/(1,1)}$.

The low formation temperature of NH_3 suggests that most of the NH_3 in the CMZ was not produced by a gas-phase reaction. If NH_3 were produced with a formation temperature of ≥ 20 K, that is, the current gas temperature, the ortho-to-para ratio should be < 1.5. Only 5% of the total integrated intensity shows $R_{\mathrm{o/p}} < 1.5$.

It should be noted that the formation temperature of NH_3 is similar to the dust temperature in the CMZ, which is estimated to be $\simeq$ 15–22 K (Lis et al. 2001). This suggests that the observed NH_3 molecules were formed on the surface of cold dust grains.

At the observed formation temperature, i.e., 11–20 K, NH_3 molecules cannot be released from the dust surface into a gas phase. Therefore, the dust should be heated up to 100 K to release the NH_3 from the dust to the gas phase, because the ice at 100 K can release NH_3 within a few years (Sandford & Allamandola 1993). The transition timescale of ortho-NH_3 and para-NH_3 is $\sim 10^6$ yr in the interstellar gas (Cheung et al. 1969). Since the observed ortho-to-para ratio is larger than the statistical equilibrium value, NH_3 would be released from the dust within the transition timescale. Therefore, the dust must be heated within $\lesssim 10^6$ yr.

4.3. Transient Heating of Dust

In the previous section, we suggested that the bulk of NH_3 gas in the CMZ must be released from the dust that was previously heated up. We attribute this heating process to the followings possibilities: interstellar shocks, direct dust collisions, a starburst, and ambipolar diffution. Considering these mechanisms, we suggest that the interstellar shocks caused by a supernova and the direct dust collisions would be possible mechanisms for our transient dust heating scenario.

We first consider the passage of an interstellar shock (Umemoto et al. 1999). For galactic disk objects, the enhancement of the ortho-to-para ratio due to an interstellar shock is supported by the NH_3 observations of the active and massive star-forming regions (Figure 9). In such a source, a strong bipolar outflow is produced, and it creates a strong shock, although the shocked region is much more compact than the CMZ. The interstellar shock can heat the interstellar gas directly. Although the gas can hardly heat the interstellar dust, accelerated electrons can heat the dust grain.

In the CMZ, there is considerable evidence suggesting the presence of an extended shocked region. The ubiquity of the intense thermal SiO lines (Martin-Pintado et al. 1997; Handa et al. 2006) and many shell structures on the *l*-*v* map observed in the CS line (Tsuboi et al. 1999) are attributed to be caused by the strong shocks passing through the entire CMZ. These shocks can transiently heat the dust.

What is the origin of the shock? Multiple supernovae (SN) shocks are the first possibility. We estimated the timescale at which SN shocks blow through the CMZ to be $\sim 10^4$ yr using the multi-phase interstellar gas model of McKee & Ostriker (1977). In this estimation, we used an SN rate of 10^{-11}–10^{-9} pc^{-3} yr^{-1} (Muno et al. 2004; Schanne et al. 2006), and the H atom density at the SN remnant interior of $n_{\mathrm{h}} = 10^{-2}$ cm^{-3} (McKee & Ostriker 1977). In the Galactic center region, the H atom density of the ambient interstellar medium is larger than that in the galactic disk region, the H atom density at the SN remnant interior may also be larger. However, even if $n_{\mathrm{h}} = 10^2$ cm^{-3}, the timescale is $\sim 10^5$ yr.

Galactic bar shock is the second possibility. The molecular gas in the CMZ should be strongly affected by a non-axisymmetric potential. The gas forms a bar-like structure, and is undergoing a strong non-circular motion (Sawada et al. 2004). In such a case, a strong shock is expected at the leading edge of the bar (e.g., Sorensen et al. 1976; Athanassoula 1992). This shock is observed in extra galaxies (e.g. Handa et al. 1990; Usero et al. 2006). We estimated the timescale at which the galactic bar shock passes through the entire CMZ to be 4×10^6 yr which is half of the rotation period at a radius of 250 pc and a velocity of 200 km s^{-1}. However, the absence of systematic structure in the ortho-to-para ratio suggests that the galactic bar does not produce the fresh NH_3.

Cloud-cloud collisions are also a possible trigger of the shock wave. The energy of turbulent motions in the clouds within 300 pc of the center is 10^{53} erg (Guesten et al. 1985). This energy is larger than the thermal energy required to heat the dust to 100 K, 10^{51} erg, which is estimated from the total dust mass in the central 400 pc of 5.3×10^7 $M_\odot$(Pierce-Price et al. 2000), and the specific heat of graphite of 1.3×10^8 erg K^{-1} g^{-1}. Cloud-cloud collisions may heat the dust surface by the transfer of energy through the shock wave. However, the timescale of cloud-cloud collisions is one order of magnitude longer than the transition timescale of NH_3, $\sim 10^6$ yr, as shown below. The collision timescale is estimated by $t_{\mathrm{col}} = 1/(n_{\mathrm{c}}\sigma_{\mathrm{c}}v_{\mathrm{c}})$, where n_{c} is the number density of clouds, σ_{c} is the collisional cross section, and v_{c} is the relative velocity. The number density of clouds is estimated from the total molecular mass in the entire CMZ of (3–8) $\times 10^7$ $M_\odot$(e.g. Tsuboi et al. 1999) and a cloud mass of 2×10^3 $M_\odot$. We use a cloud radius of 1 pc and a H_2 number density of 10^4 cm^{-3} in this estimation because clouds with a size of several pc are observed in the CS maps of Tsuboi et al. (1999), and the critical density of CS is 10^4 cm^{-3}. The collisional cross section is $\sigma_{\mathrm{c}} \sim 10^{37}$ cm^2 at a cloud radius of 1 pc. The relative velocity of clouds is assumed to be $v_{\mathrm{c}} \sim 10$ km s^{-1}. The timescale of cloud-cloud collisions is estimated to be $\sim 10^7$ yr from these values. The comparison of the timescales suggests that cloud-cloud collisions cannot heat the dust frequently enough.

The direct collision of dust particles is the second mechanism. The dust surface is heated to $\sim 10^3$ K when all of the collisional energy is transferred to the heating energy of dust. In this mechanism, the dust particles must collide within the conversion timescale of ortho-NH_3 and para-NH_3. The collision timescale is estimated by $t_{\rm col} = 1/(n_{\rm d}\sigma_{\rm d}v_{\rm d})$, where $n_{\rm d}$ is the number density of dust particles, $\sigma_{\rm d}$ is the collisional cross section, and v_d is the turbulent velocity. The total dust mass within the central 400 pc is 5.3×10^7 $M_\odot$(Pierce-Price et al. 2000), and the mass of a dust particle is estimated to be 6×10^{-12} g for a dust particle radius of 1 μm and mass density of charcoal powder of 1.5 g cm^{-3}. Therefore, the number density is estimated to be $n_{\rm d} \sim 10^{-10}$ cm^{-3}. This is an average value over the entire CMZ. The collisional cross section is $\sigma_{\rm d} \sim 10^{-8}$ cm^2 at a radius of 1 μm. The turbulent velocity is assumed to be $v_{\rm d} \sim 10$ km s^{-1}. Using these values, we estimated $t_{\rm col} \sim 10^4$ yr. This timescale is upper limit. If the dust is concentrated in the core of each cloud with the same turbulent motion, $n_{\rm d}$ is larger and it gives shorter $t_{\rm col}$. Before the grains collide directly, the gas clouds that contain dust particles collide with each other. In this case, the dust particles can slow down before the direct collision. However they are also affected by gas drag, which heats up the dust. Therefore, the conclusion remains valid, unless the dust particles are tightly bounded in the molecular clouds by the gas drag. In this case, the discussion should be the same as that of cloud-cloud collisions. The comparison of timescales suggests that the direct collision of dust particles is a possible heating mechanism.

Another heating mechanism is a transient starburst. When a dust particle is heated up to 100 K by strong UV radiation, NH_3 molecules are released in the interstellar space. There is substantial evidence that indicates a burst of star formation in the Galactic center. However, this occurred 10^7–10^9 years ago (Yasuda et al. 2008 and reference therein). This timescale is much longer than the transition timescale of NH_3. Therefore, a transient starburst could not have heated the dust.

The last mechanism is an ambipolar diffusion. Hüttemeister et al. (1993) suggested that the gas can be heated up to $\sim$ 200 K by collisions between neutrals and ions under a magnetic field strength of 500 μG. However, this mechanism does not work well in our transient heating scenario. The energy of collision between the dust particle and an ion is fifteen order of magnitude smaller than that of direct dust collision. The collisional energy is too small to heat the dust to a sufficient temperature to release the NH_3, 100 K. Therefore, the dust could not been heated by ambipolar diffusion,

Our model requires the heating to have occurred within $\lesssim 10^6$ yr. Therefore, SN shocks, galactic shocks, and direct dust collisions are possible. However, our estimation of the cooling timescale of molecular gas, which is described in the next subsection, indicates that the timescale should be $\sim 10^5$ yr. Therefore, a galactic shock that occurred $\sim 10^6$ yr ago is not preferable. We therefore conclude that SN shocks and direct dust collisions would be possible mechanisms for our transient dust heating scenario, and both mechanisms can produce fresh NH_3 from the dust grains.

We expect that there should be the difference of the spatial distributions in the SN shocks and the direct dust collisions. In the case of the SN shocks, the dust would be heated in the shocked layer. In the case of the direct dust collisions, individual heating spot is the fairly smaller scale of dust particles. These minor heated dusts are mixed with the major cool dusts in the observed beam, therefore they are uniformly observed as cold dusts. Submillimeter wave observations with very high resolution could find the differences of the distributions between two mechanisms.

4.4. *Cooling Timescales of Gas and Dust*

NH_3 is released from the dust grains to the gas-phase at a sublimation temperature of ~ 100 K. Therefore, the dust should be heated up to to ~ 100 K in the case that NH_3 molecules are released from the dust. The observed gas temperature is close to this temperature. However, the observed dust temperature is much lower.

To resolve this discrepancy, we hypothesize that the interstellar matter in the Galactic center region is not in thermal equilibrium. The dust is believed to heat the gas through the photoelectric process, however, the gas cannot heat the dust. Therefore, our hypothesis would be confirmed if the cooling timescale of gas is much longer than that of dust.

We estimated the timescale in which the gas is cooled from 100 to 10 K. The main cooling process of the gas in this temperature range is CO emission. The cooling timescale of gas is estimated to be $\sim 10^5$ yr from the thermal energy of $Q = 5/2k\Delta T \sim 10^{-14}$ erg and the CO cooling rate of $\sim 10^{-27}$ erg s^{-1} (Hegmann et al. 2007).

We estimated the timescale in which the dust is cooled from 100 to 10 K. The major cooling process of the dust in this temperature range is black body radiation. The thermal energy of the dust with temperature $T(t)$ at time t is given by

$$Q(t) = \frac{4\pi}{3}a^3\rho c T(t) \tag{1}$$

where a, ρ, and c denote the radius, density, and specific heat of dust. The cooling rate of the dust by the black body radiation is given by

$$\frac{dQ(t)}{dt} = -4\pi a^2 \sigma [T(t)]^4 \tag{2}$$

where σ is the Stefan-Boltzmann constant. Using these equations, we found the cooling timescale of dust from 100 to 10 K to be $t \sim 10^{-3}$ yr for $a = 1\mu$m, $\rho = 1.5$ g cm^{-3} as the mass density of charcoal powder, and $c = 1.3 \times 10^8$ erg K^{-1} g^{-1} as the specific heat of the graphite.

The cooling timescale of the gas is 7 orders of magnitude longer than that of the dust. Therefore, transient heating of the interstellar matter occurred in the past, and the observed temperature difference between the gas and the dust can be observed soon after the heating. This may explain why temperature of molecular gas is much higher than that of the dust.

4.5. Individual Clouds

4.5.1. Overview of Clouds in the CMZ

We estimated the physical parameters of the identified 13 clouds under the optically thin assumption. The calculated rotational temperatures, column densities, and ortho-to-para ratios are listed in Table 3.

With regard to the clouds in the CMZ, the virial masses observed in the CO line are one order of magnitude larger than the mass derived from the CO luminosity with a standard conversion factor (Oka et al. 1998). This suggests that the clouds in the CMZ may not be gravitationally bound and are instead in pressure equilibrium with the hot gas or magnetic field in this region. However, the cloud observed in the NH_3 line may not be affected by the external pressure because the NH_3 line would trace a different density range.

Therefore, we investigate the virial mass and luminosity mass in the NH_3 line. Using the abundance ratio of $X(NH_3) = 10^{-9}$ (Hüttemeister et al. 1993) and spherically symmetric geometry, the H_2 number densities are derived from the luminosity masses to be $n(H_2) \sim 10^3$–10^4 cm^{-3}, as given in Table 3. These values are consistent with the NH_3 critical density, suggesting that the estimated luminosity masses are valid. We estimated the luminosity mass, $M_{\rm lum}$, from the integration of the column densities, and the virial mass, $M_{\rm vir}$, from the apparent size with the beam deconvolution and the observed line width. We summarize these values of the 13 clouds in Table 3 and show the $M_{\rm lum}$-$M_{\rm vir}$ plot in Figure 10. The luminosity mass and virial mass of nine clouds are consistent with an order of magnitude. This implies that most of the molecular clouds traced by the NH_3 line are roughly in virial equilibrium. The external pressure affects only the less dense gas traced by the CO line.

Only four clouds (ID 1, 3, 6, and 8) appear to not be in the virial equilibrium, although there are reasons in each case, as given below. In the *l*-*v* diagram, these clouds do not lie on the main ridge that indicates the main rotating component of the Milky Way Galaxy. The rotational temperature and the ortho-to-para ratio of these clouds are different from those of the other clouds. We summarize the features of these four unvirialized clouds as follows.

4.5.2. Cloud 1

Cloud 1 is located at the western edge of the observed area and at $v_{\rm LSR} \simeq 0$ km s^{-1}. The velocity and angular extent suggest that cloud 1 may be located in the Galactic disk. The annihilation source 1E1740.7-2942 is located close to the cloud in the sky. Bally & Leventhal (1991) assumed that the source is not associated to the 0 km s^{-1} component because it should not be in the Galactic center region. However, the rotational temperature of 45 ± 4 K is higher than that of the disk clouds and close to that of the clouds in the Galactic center. Therefore, we conclude that cloud 1 may be located at the Galactic center region. In a higher-resolution map in the CS line (Tsuboi et al. 1999), two clouds are observed at the position of cloud 1. In the case that these clouds are gravitationally unbound, our estimation of the virial mass is overestimated and the large discrepancy between the two masses is not real.

4.5.3. Cloud 3

Cloud 3 is located at Sgr C in the sky. The peak velocity in the NH_3 line of $v_{\rm LSR} \simeq -53$ km s^{-1} is close to the central velocity in the H91α and H109α recombination lines of $v_{\rm LSR} \simeq -59$ km s^{-1} (Pauls & Mezger 1975; Anantharamaiah & Yusef-Zadeh 1989). This suggests that the Sgr C H II region is physically associated. It interacts with the molecular cloud and ionizes a part of it. The rotational temperature of 45 ± 3 K is higher than that of other clouds in the CMZ. This suggests that cloud 3 is heated by the H II region and it is expanding rapidly due to the active star formation.

4.5.4. Cloud 6

Cloud 6 is located at high Galactic latitude ($b \simeq 0.15$) at $v_{\rm LSR} \sim 106$ km s^{-1}. It is redshifted approximately 60 km s^{-1} from the Sgr A 50 km s^{-1} cloud, which is located at the same longitude. This cloud appears as a shell-like structure on the *l*-*v* map in the CS line (Tsuboi et al. 1999). Soft X-ray (1–3 keV) emission is detected at the position of this cloud (Wang et al. 2002). These suggest that this cloud is associated with a newly identified supernova remnant. The large virial mass should be due to expansion of this SN remnant. The kinetic energy is 10^{51} erg when cloud 6 is expanding with a mass of $M_{\rm lum} = 2.1 \times 10^5$ $M_\odot$and an expansion velocity of $\Delta v/2 = 17$ km s^{-1}. This energy is comparable to the kinetic energy of the stellar wind from a 60–100 $M_\odot$star (Abbott 1982) and less than that of a hypernova explosion (Iwamoto et al. 1998).

4.5.5. Cloud 8

Cloud 8 is the same structure reported in Paper I. The rotational temperature and the number density of this cloud are higher than those of other clouds. The location of this cloud is close to that of the $0.^\circ 9$ anomaly reported from the observation in CO line (Oka et al. 2007). The features of high temperature and density are similar to the $0.^\circ 9$ anomaly. Although the highly blue-shifted component ($v_{\rm LSR} = -120$ km s^{-1}) is detected in CO line, we could not detect this component.

This cloud is unresolved by the Kagoshima 6 m telescope beam. However, it could be resolved by a high resolution observation using the Kashima 34 m telescope. Figures 11 and 12 show the *l*-*v* and *b*-*v* maps obtained using the Kashima 34 m telescope. In this higher-resolution observation, the cloud is resolved into three components. The peak positions, apparent sizes, and line widths of these components are shown in Table 4.

We call these three components 8a, 8b, and 8c in the order of the galactic longitude. Cloud 8 has a large virial mass because it is an unbound system. The rotational temperatures of all components are similar, and they are higher than the mean temperature of the CMZ. The location and velocity of components 8c is close to the high velocity compact cloud, CO 0.88−0.08 (Oka et al. 2007). These would be the same structure. However, the component 8a and 8b are not detected in CO line (Oka et al. 2007). This would be because the CO line is affected by foreground absorption. We summarize the physical parameters of three components that have been obtained under the optically thin assumption in Table 5. Their virial masses are the same as their luminosity masses within a factor of $\simeq 2$.

5. Conclusions

We have presented a map of the major part of the CMZ by simultaneous observations in the NH_3 $(J, K) = (1,1)$, (2,2), and (3,3) lines using the Kagoshima 6 m telescope. Our observations are summarized as follows:

1. We obtained the ortho-to-para ratio of NH_3 in the CMZ to be 1.5–3.5 using the rotation diagram method. This ratio is higher than that of galactic disk clouds, and as same as those of the active and massive star forming regions and the centers of nearby external galaxies.
2. An ortho-to-para ratio of 1.5–3.5 corresponds to a formation temperature of 11–20 K. The formation temperature is very close to the temperature of dust. NH_3 in the CMZ has been produced on the cold dust grains and released into the gas phase by SN shocks or direct dust collisions.
3. The discrepancy between warm molecular gas and cold dust can be explained by transient heating of the interstellar media in the CMZ on a timescale 10^5 years. NH_3 molecules were released from the dust on this timescale.
4. We present the physical conditions of the 13 clouds identified in the NH_3 map. For a majority of the clouds in the CMZ, the luminosity mass and the virial mass are consistent in an order of magnitude.

We thank an anonymous referee for very useful comments. We also thank Dr. Mark Morris for his invaluable comments about the direct dust collisions. We also thank K. Takeda, a graduate from Kagoshima University, for his technical support in the observations. We acknowledge S. Takano and T. Umemoto, NRO, for their scientific advice. We also acknowledge E. Kawai, NiCT, and T. Miyaji and K. Miyazawa, NAOJ, for their technical supports in the observations. T.O. was supported by a Grant-in-Aid for Scientific Research from the Japan Society for the Promotion of Science (17340055). T.H. thanks the Japan Society for the Promotion of Science for the financial support provided by the JSPS Grant-in-Aid for S (17104002).

References

Abbott, D. C. 1982, ApJ, 263, 723
Anantharamaiah, K. R., & Yusef-Zadeh, F. 1989, The Center of the Galaxy, 136, 159
Athanassoula, E. 1992, MNRAS, 259, 345
Bally, J., & Leventhal, M. 1991, Nature, 353, 234
Cheung, A. C., Rank, D. M., Townes, C. H., Knowles, S. H., & Sullivan, W. T., III 1969, ApJL, 157, L13
Dahmen, G., Huttemeister, S., Wilson, T. L., & Mauersberger, R. 1998, A&A, 331, 959
Gómez, Y., Rodríguez-Rico, C. A., Rodríguez, L. F., & Garay, G. 2000, Revista Mexicana de Astronomia y Astrofisica, 36, 161
Guesten, R., Walmsley, C. M., Ungerechts, H., & Churchwell, E. 1985, A&A, 142, 381
Guesten, R., & Fiebig, D. 1988, A&A, 204, 253
Handa, T., Nakai, N., Sofue, Y., Hayashi, M., & Fujimoto, M. 1990, PASJ, 42, 1
Handa, T., Sakano, M., Naito, S., Hiramatsu, M., & Tsuboi, M. 2006, ApJ, 636, 261
Ho, P. T. P., Barrett, A. H., Myers, P. C., Matsakis, D. N., Chui, M. F., Townes, C. H., Cheung, A. C., & Yngvesson, K. S. 1979, ApJ, 234, 912
Ho, P. T. P., Moran, J. M., & Rodriguez, L. F. 1982, ApJ, 262, 619
Hegmann, M., Kegel, W. H., & Sedlmayr, E. 2007, A&A, 469, 223
Hüttemeister, S., Wilson, T. L., Bania, T. M., & Martin-Pintado, J. 1993, A&A, 280, 255
Iwamoto, K., et al. 1998, Nature, 395, 672
Kutner, M. L., & Ulich, B. L. 1981, ApJ, 250, 341
Lis, D. C., Serabyn, E., Zylka, R., & Li, Y. 2001, ApJ, 550, 761
Martin-Pintado, J., de Vicente, P., Fuente, A., & Planesas, P. 1997, ApJL, 482, L45
Matsakis, D. N., Bologna, J. M., Schwartz, P. R., Cheung, A. C., & Townes, C. H. 1980, ApJ, 241, 655
Mauersberger, R., Wilson, T. L., Walmsley, C. M., Henkel, C., & Batrla, W. 1985, A&A, 146, 168
Mauersberger, R., Henkel, C., Weiß, A., Peck, A. B., & Hagiwara, Y. 2003, A&A, 403, 561
McKee, C. F., & Ostriker, J. P. 1977, ApJ, 218, 148
Morris, M., Polish, N., Zuckerman, B., & Kaifu, N. 1983, AJ, 88, 1228
Muno, M. P., et al. 2004, ApJ, 613, 326
Nagayama, T., Omodaka, T., Handa, T. Iahak, H. B. H., Sawada, T., Miyaji, T., & Koyama, Y. 2007, PASJ, 59, 869
Nagayama, T., et al., 2008, in preparation
Nakajima, T. et al., 2007, PASJ, 59, 1005
Oka, T., Hasegawa, T., Hayashi, M., Handa, T., & Sakamoto, S. 1998, ApJ, 493, 730
Oka, T., Nagai, M., Kamegai, K., Tanaka, K., & Kuboi, N. 2007, PASJ, 59, 15
Pauls, T., & Mezger, P. G. 1975, A&A, 44, 259
Pierce-Price, D., et al. 2000, ApJL, 545, L121
Sandford, S. A., & Allamandola, L. J. 1993, ApJ, 417, 815
Sawada, T., et al. 2001, ApJS, 136, 189
Sawada, T., Hasegawa, T., Handa, T., & Cohen, R. J. 2004, MNRAS, 349, 1167
Schanne, S., Casse, M., Sizun, P., Cordier, B., & Paul, J. 2006, ArXiv Astrophysics e-prints, arXiv:astro-ph/0609566
Schwartz, P. R., Bologna, J. M., & Waak, J. A. 1978, ApJ, 226, 469
Sorensen, S.-A., Matsuda, T., & Fujimoto, M. 1976, Ap&SS, 43, 491
Takano, S., Nakai, N., Kawaguchi, K., & Takano, T. 2000, PASJ, 52, L67
Takano, S., Nakai, N., & Kawaguchi, K. 2002, PASJ, 54, 195
Takano, S., Nakanishi, K., Nakai, N., & Takano, T. 2005, PASJ, 57, L29
Tieftrunk, A. R., Megeath, S. T., Wilson, T. L., & Rayner, J. T. 1998, A&A, 336, 991
Tsuboi, M., Handa, T., & Ukita, N. 1999, ApJS, 120, 1

Umemoto, T., Mikami, H., Yamamoto, S., & Hirano, N. 1999, ApJL, 525, L105
Usero, A., García-Burillo, S., Martín-Pintado, J., Fuente, A., & Neri, R. 2006, A&A, 448, 457
Usero, A., García-Burillo, S., Martín-Pintado, J., Fuente, A., & Neri, R. 2007, New Astronomy Review, 51, 75
Wang, Q. D., Gotthelf, E. V., & Lang, C. C. 2002, Nature, 415, 148
Weiß, A., Neininger, N., Henkel, C., Stutzki, J., & Klein, U. 2001, ApJL, 554, L143
Wilson, T. L., & Mauersberger, R. 1990, A&A, 239, 305
Yasuda, A., Nakagawa, T., Spaans, M., Okada, Y., & Kaneda, H. 2008, A&A, 480, 157

Table 1. Molecular clouds toward the Galactic center identified in the NH_3 line.

ID	l (°)	b (°)	$v_{\rm LSR}$ (km s^{-1})	Δl (°)	Δb (°)	Δv (km s^{-1})	Comments
1	−0.86	−0.11	−10	...	0.21	53	at the western edge of the observed area
2	−0.86	0.00	141	0.20	0.17	31	a part of EMR
3	−0.51	−0.15	−53	0.17	0.16	39	associated with Sgr C
4	−0.11	−0.07	21	0.21	0.16	49	Sgr A 20 km s^{-1} cloud
5	0.07	−0.08	48	0.23	0.15	49	Sgr A 40 km s^{-1} cloud
6	0.07	0.15	106	0.16	0.19	33	
7	0.74	−0.13	39	0.34	0.27	65	Sgr B cloud complex
8	0.78	−0.12	22	...	0.16	56	0.°9 wing feature*
9	0.97	−0.10	80	0.31	0.19	37	
10	1.24	−0.07	83	0.43	0.35	49	the 1.°3 cloud complex
11	1.53	−0.23	−25	0.23	0.17	37	
12	1.60	−0.07	50	...	0.24	29	
13	1.70	−0.37	−35	0.18	...	27	

* defined in Paper I

Table 2. The integrated intensity of 13 clouds.

ID	$\int T_{\rm MB} dv$ (K km s^{-1})	fraction* (%)
1	90	1.8
2	12	0.2
3	59	1.2
4	305	6.1
5	434	8.7
6	58	6.1
7	1224	24.6
8	107	2.2
9	246	5.0
10	562	11.3
11	135	2.7
12	151	3.1
13	64	1.3
total	3447	69.4

* The fraction of the total integrated intensity of the entire observed area ($\int T_{\rm MB} dv = 4972$ K km s^{-1}).

Table 3. Physical properties of the 13 clouds.

ID	$T_{\rm rot}$	N(ortho)	N(para)	N(total)	$R_{\rm o/p}$	$T_{\rm form}$	d	$n(H_2)$	$M_{\rm lum}$	$M_{\rm vir}$
	(K)		10^{14} (cm^{-2})			(K)	(pc)	10^4 (cm^{-3})	10^6 ($M_\odot$)	10^6 ($M_\odot$)
1	45 ± 3	1.8 ± 0.2	1.69 ± 0.09	3.5 ± 0.3	1.1 ± 0.2	≥ 24	21	0.55	1.2	7.2
2	31 ± 2	2.9 ± 0.6	1.08 ± 0.07	3.9 ± 0.6	2.6 ± 0.7	13 ± 3	13	0.98	0.56	1.6
3	46 ± 2	2.6 ± 0.2	2.52 ± 0.09	5.2 ± 0.3	1.0 ± 0.1	≥ 32	6	2.8	0.15	1.1
4	33 ± 1	16.1 ± 0.8	5.99 ± 0.10	22.1 ± 0.9	2.7 ± 0.2	12 ± 1	9	8.2	1.4	2.6
5	37 ± 1	13.0 ± 0.5	6.83 ± 0.10	19.8 ± 0.6	1.9 ± 0.1	16 ± 2	15	4.2	3.8	4.6
6	32 ± 2	3.0 ± 0.5	1.35 ± 0.07	4.4 ± 0.5	2.2 ± 0.5	14 ± 3	8	1.9	0.21	1.0
7	37 ± 1	26.6 ± 0.5	14.2 ± 0.11	40.8 ± 0.6	1.9 ± 0.1	16 ± 1	38	3.5	49	20
8	43 ± 1	10.2 ± 0.3	6.86 ± 0.10	17.0 ± 0.4	1.5 ± 0.1	20 ± 2	4	15	0.20	1.5
9	41 ± 1	7.3 ± 0.3	4.88 ± 0.09	12.2 ± 0.4	1.5 ± 0.1	20 ± 2	25	1.6	6.3	4.3
10	33 ± 1	10.6 ± 0.6	4.36 ± 0.09	15.0 ± 0.7	2.4 ± 0.2	13 ± 1	52	0.93	34	16
11	39 ± 2	3.7 ± 0.3	2.04 ± 0.08	5.7 ± 0.4	1.8 ± 0.2	17 ± 2	15	1.2	1.1	2.6
12	31 ± 1	11.4 ± 0.8	4.36 ± 0.09	15.7 ± 0.8	2.6 ± 0.2	13 ± 1	27	1.9	9.4	2.8
13	33 ± 2	5.3 ± 0.6	2.04 ± 0.09	7.3 ± 0.7	2.6 ± 0.4	13 ± 2	13	1.9	1.0	1.2

Table 4. Three components of the 0.°9 wing feature observed using Kashima 34 m telescope.

ID	l	b	$v_{\rm LSR}$	Δl	Δb	Δv
	(°)	(°)	(km s^{-1})	(°)	(°)	(km s^{-1})
8a	0.767	−0.030	25	0.065	0.065	28
8b	0.775	−0.098	22	0.077	0.090	29
8c	0.854	−0.059	10	0.061	0.067	35

Table 5. Physical properties of the three components of the 0.°9 wing feature.

ID	$T_{\rm rot}$	N(ortho)	N(para)	N(total)	$R_{\rm o/p}$	$T_{\rm form}$	d	$n(H_2)$	$M_{\rm lum}$	$M_{\rm vir}$
	(K)		10^{14} (cm^{-2})			(K)	(pc)	10^4 (cm^{-3})	10^6($M_\odot$)	10^6($M_\odot$)
8a	40 ± 1	14.7 ± 0.6	9.98 ± 0.18	24.7 ± 0.8	1.9 ± 0.1	16 ± 1	9	9.1	1.6	0.86
8b	40 ± 1	15.4 ± 0.6	10.7 ± 0.18	26.1 ± 0.8	1.5 ± 0.1	20 ± 2	12	7.3	3.0	1.2
8c	37 ± 1	19.6 ± 1.1	9.11 ± 0.21	28.7 ± 1.3	2.2 ± 0.2	14 ± 1	9	11	1.8	1.3

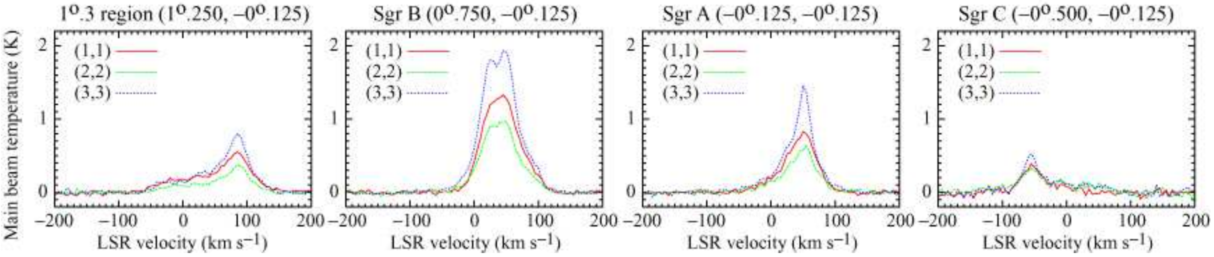

Fig. 1. The NH_3 (1,1) (red), (2,2) (green), and (3,3) (blue) spectra toward four positions of the observed area, Sgr C $(l,\ b) = (-0.^{\circ}500,\ -0.^{\circ}125)$, Sgr A $(0.^{\circ}125,\ -0.^{\circ}125)$, Sgr B $(0.^{\circ}750,\ -0.^{\circ}125)$, and $1.^{\circ}3$ region $(1.^{\circ}250,\ -0.^{\circ}125)$. Spectra are shown with the veolcity resolution of 5 km s^{-1} and on a $T_{\rm MB}$ scale.

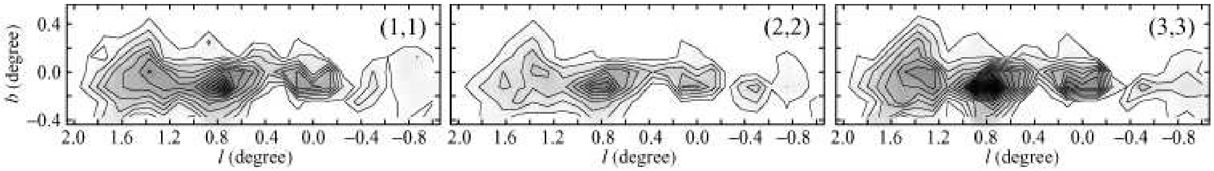

Fig. 2. Integrated intensity maps of NH_3 (1,1) (left), (2,2) (middle), and (3,3) (right). The lowest contour and the contour interval are 2,2 and 4.4 K km s^{-1} in $\int T_{\rm MB} dv$, respectively. The velocity range of the integration is $-200 \leq v_{\rm LSR} \leq 200$ km s^{-1}.

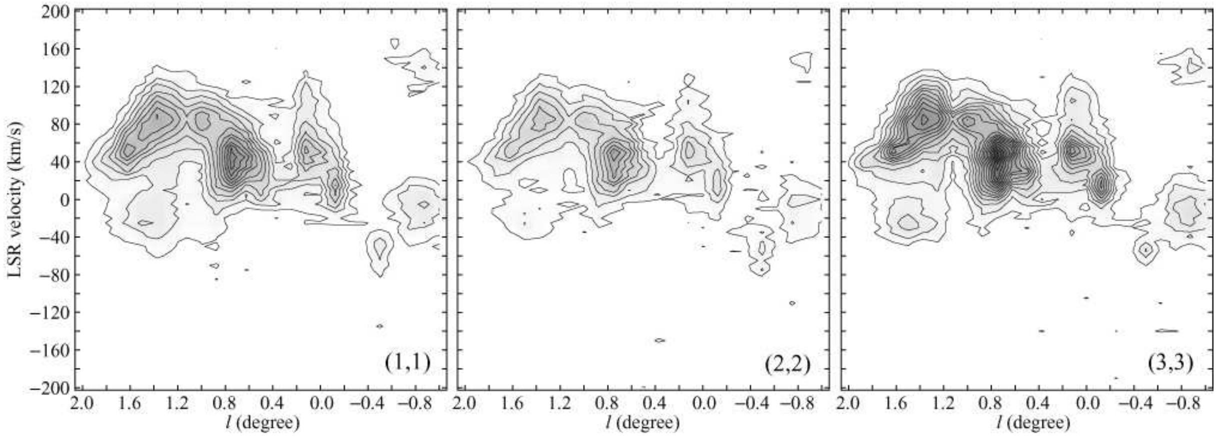

Fig. 3. Longitude-velocity (l-v) diagrams of NH_3 (1,1) (left), (2,2) (middle), and (3,3) (right) emission integrated over the entire observed latitude. The lowest contour and the contour interval are 0.25 and 0.31 K, respectively.

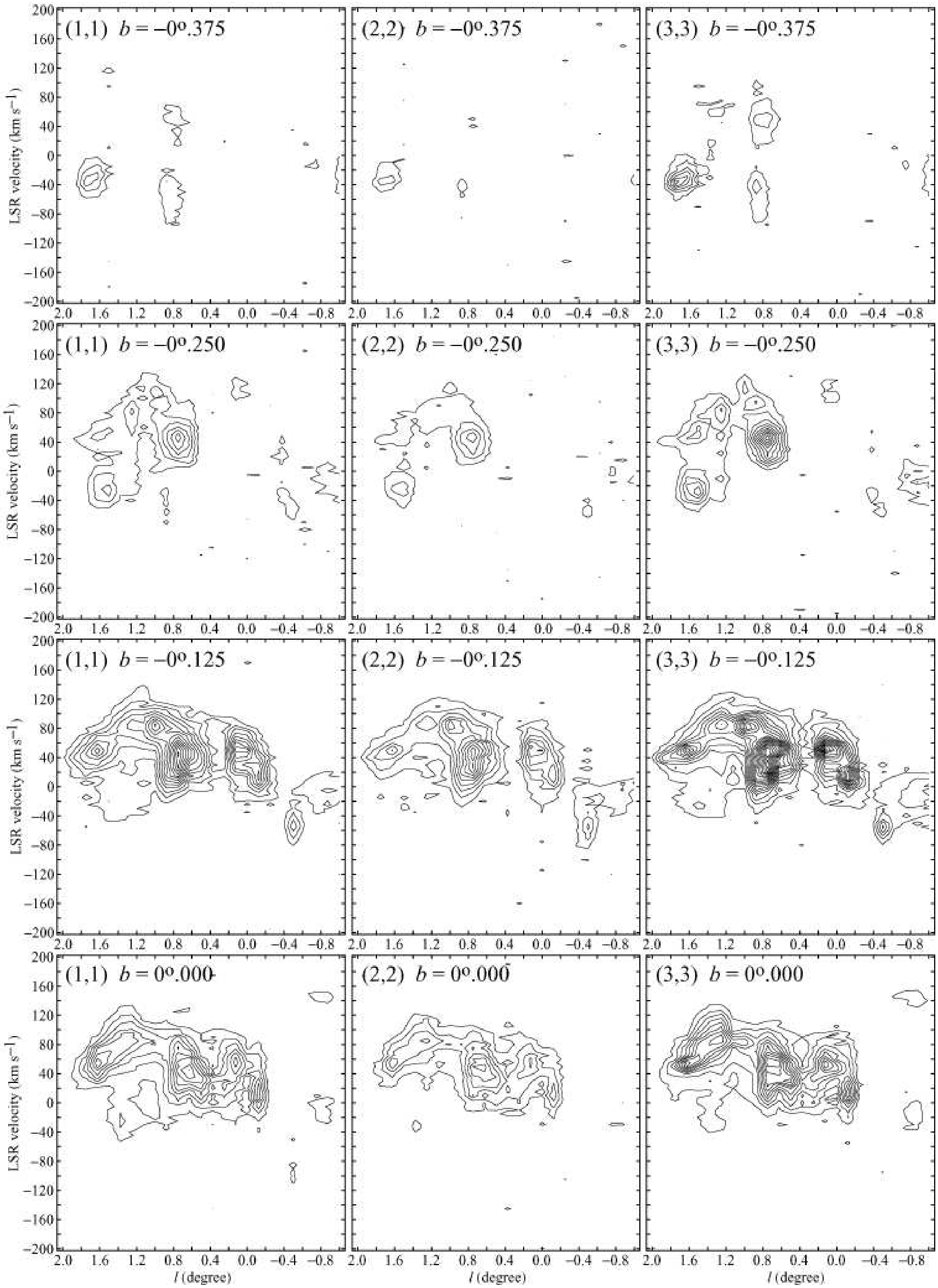

Fig. 4. Longitude-velocity (*l*-*v*) diagrams of the NH_3 (1,1) (left), (2,2) (middle), and (3,3) (right) lines. Both of the lowest contour and the contour interval are 0.1 K.

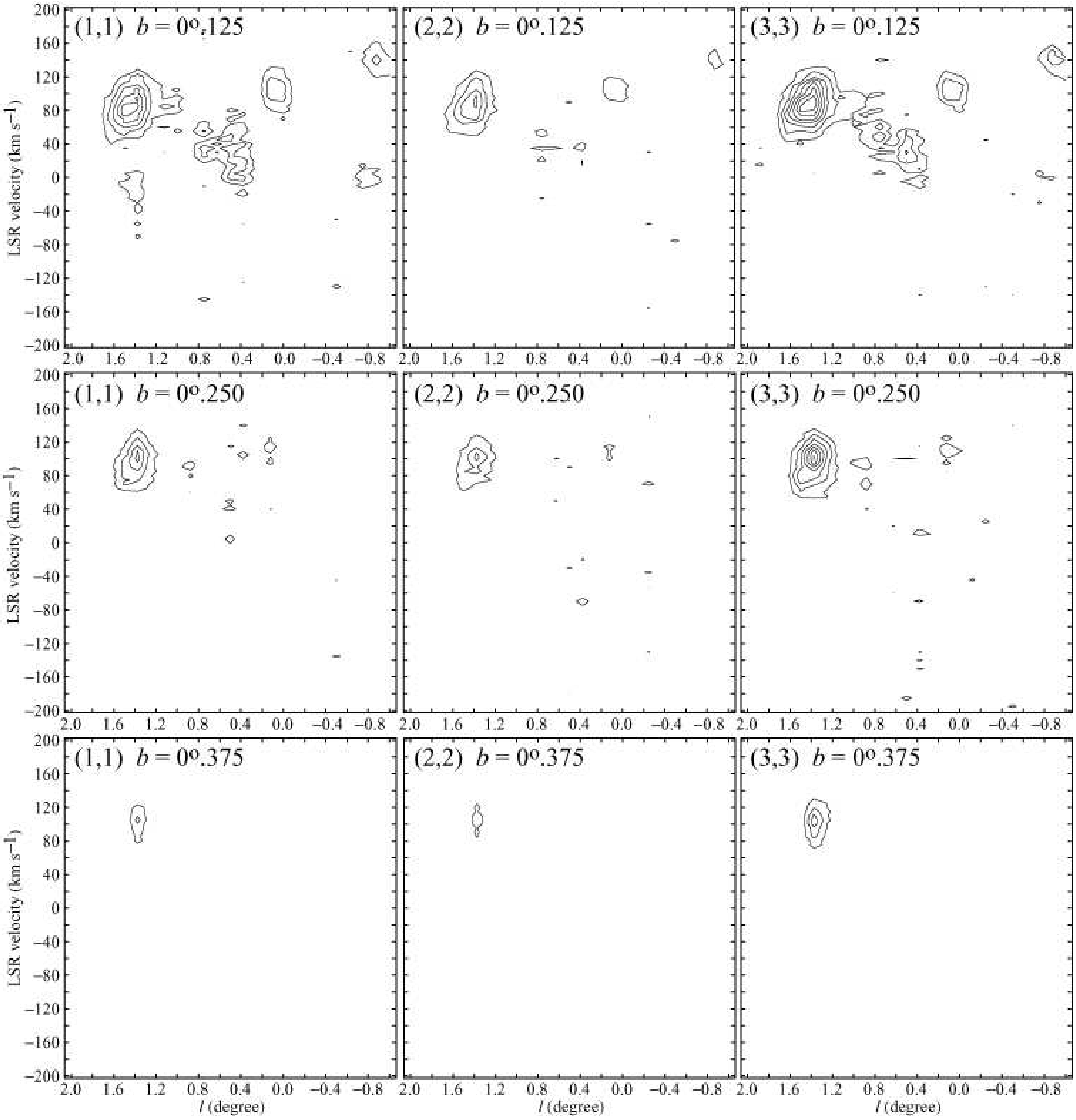

Fig. 4. Continued

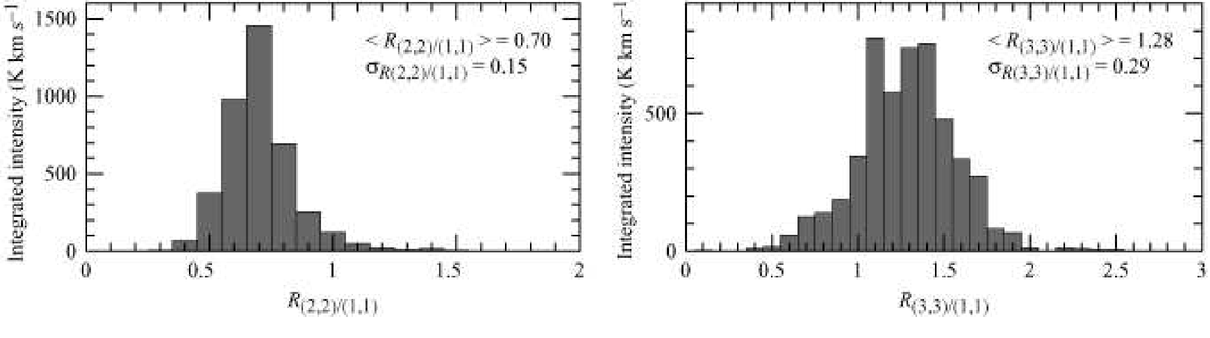

Fig. 5. Histograms of the intensity ratios of (2,2) to (1,1) (left), and (3,3) to (1,1) (right). We count the l-b-v pixels at which the lines were detected above the 3 σ level after smoothing at 10 km s^{-1}.

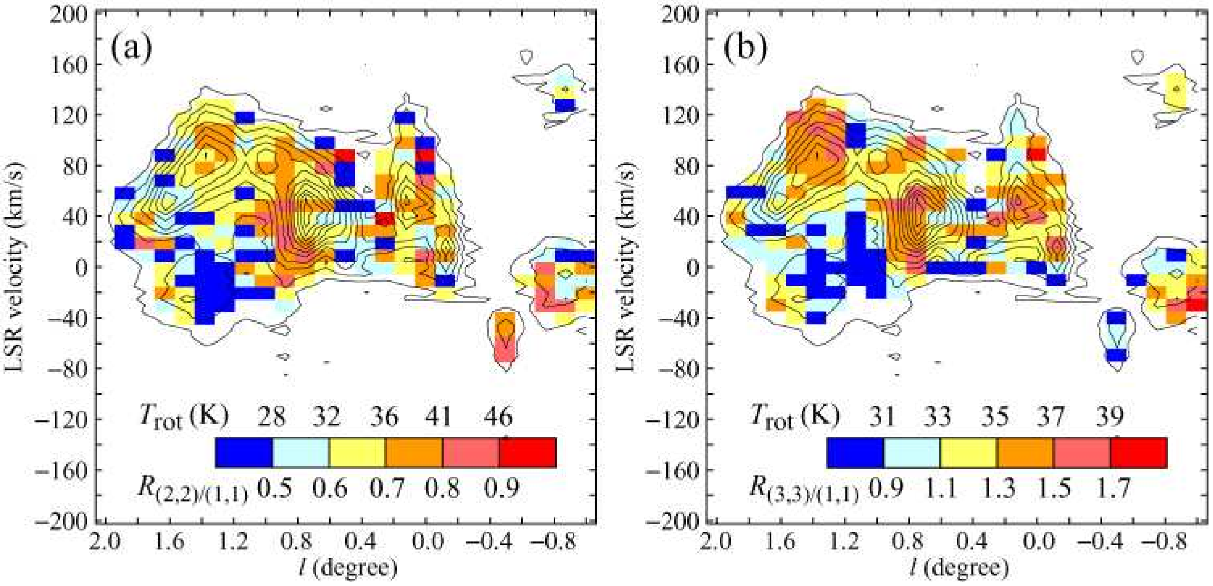

Fig. 6. The distributions of $R_{(2,2)/(1,1)}$ (a) and $R_{(3,3)/(1,1)}$ (b) superimposed on the NH$_3$ (1,1) emission integrated over the entire observed latitude. $T_{\rm rot}$ in (a) is derived for the optically thin case. $T_{\rm rot}$ in (b) is derived for the optically thin case and an ortho-to-para ratio of 2.0.

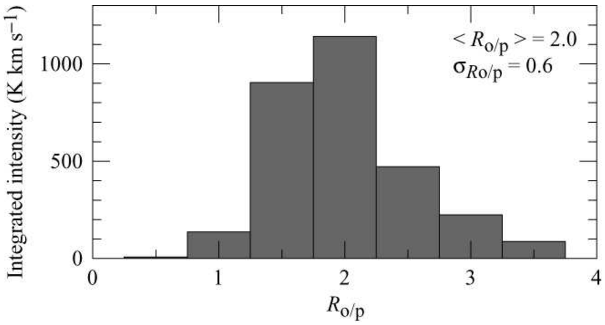

Fig. 7. The histogram of the ortho-to-para ratio. We count the l-b-v pixels at which the lines were detected above the 10 σ level after smoothing at 10 km s^{-1}.

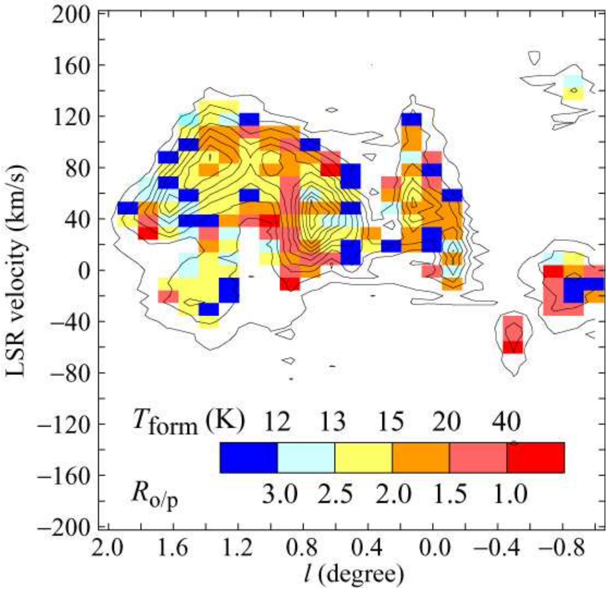

Fig. 8. The distributions of $R_{\rm o/p}$ superimposed on the NH$_3$ (1,1) emission integrated over the entire observed latitude.

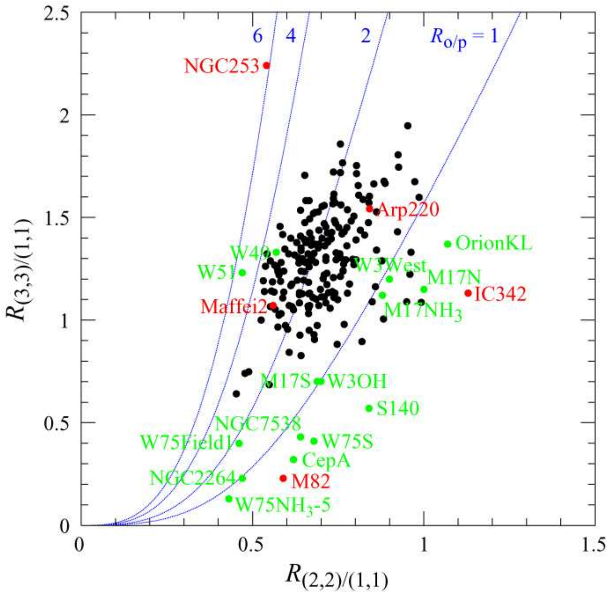

Fig. 9. The $R_{(2,2)/(1,1)}$–$R_{(3,3)/(1,1)}$ correlation plot of the CMZ (black), galactic disk clouds (green), and the central region of some external galaxies (red). For the CMZ, the spectral data detected over the 10 σ level after smoothing at 10 km s^{-1} are plotted. The data of galactic disk clouds and external galaxies are referred to from the following; Cep A (Ho et al. 1982); M17 N, M17 NH$_3$, and M17 S (Guesten & Fiebig 1988); NGC 2264 and NGC 7538 (Nagayama et al. 2008 in prep.); Orion KL (Ho et al. 1979); S140 (Mauersberger et al. 1985); W3 West and W3 OH (Tieftrunk et al. 1998); W49 (Nagayama et al. 2008 in prep.); W51 (Matsakis et al. 1980); W75 Field 1, W75 NH$_3$-5, and W75 S (Wilson & Mauersberger 1990); Arp 220 (Takano et al. 2005); IC 342 (Mauersberger et al. 2003); Maffei 2 (Takano et al. 2000); M82 (Weiß et al. 2001); NGC 253 (Takano et al. 2002); Arp 220 is plotted from the ratio of optical depths in the absorption lines.

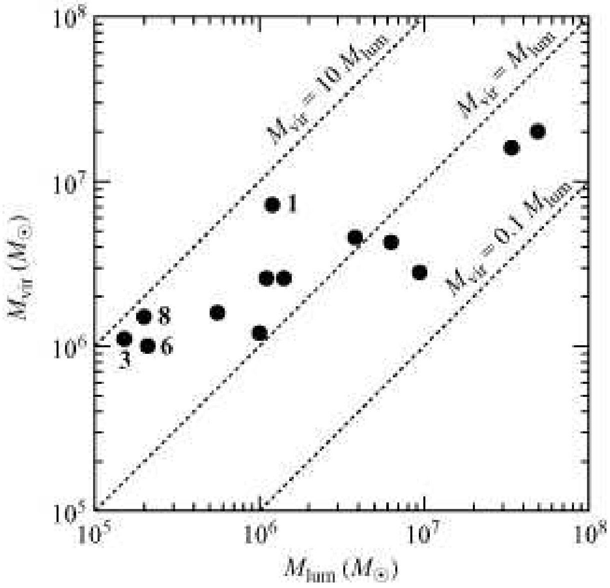

Fig. 10. The luminosity mass-virial mass plot for the 13 clouds.

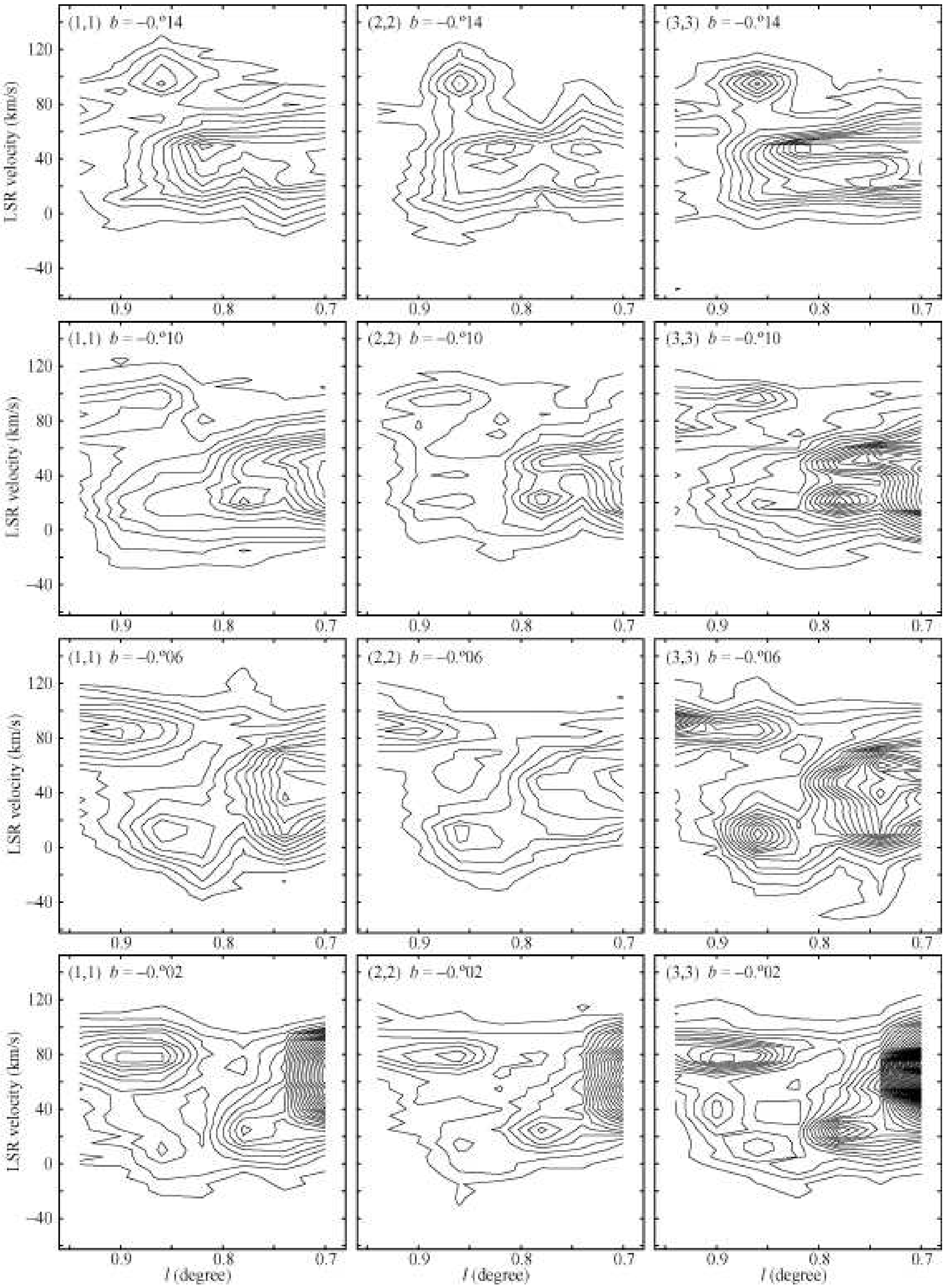

Fig. 11. High-resolution l-v diagrams of cloud 8 observed using the Kashima 34 m telescope in the NH_3 (1,1) (left), (2,2) (middle), and (3,3) (right) lines. Both the lowest contour and the contour interval are 0.2 K.

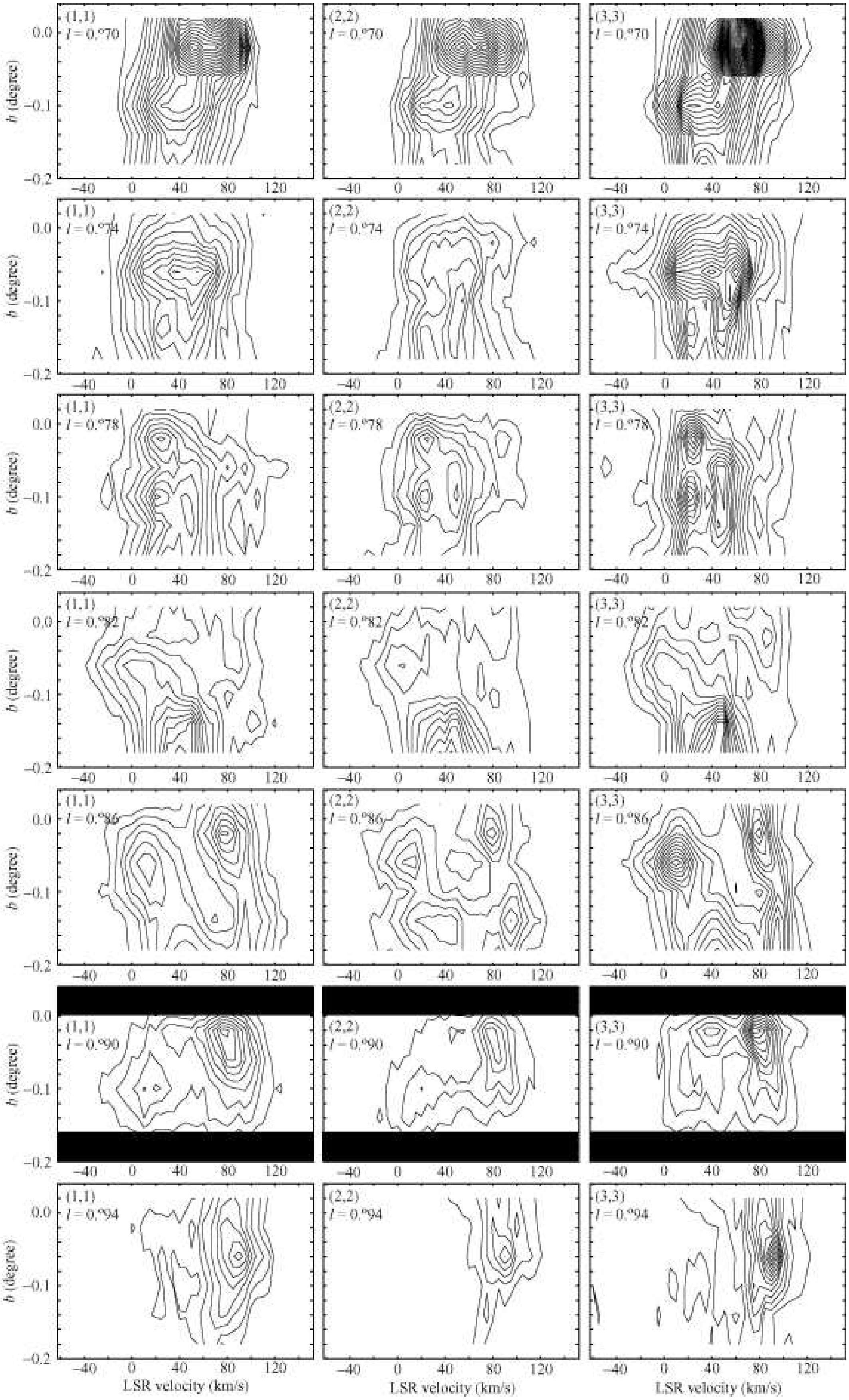

Fig. 12. High-resolution b-v diagrams of cloud 8 observed using the Kashima 34 m telescope in the NH$_3$ (1,1) (left), (2,2) (middle), and (3,3) (right) lines. Both the lowest contour and the contour interval are 0.2 K.